

## Probing Rashba spin-orbit coupling by subcycle lightwave control of valley polarization

Yu Chen,<sup>1,2</sup> Candong Liu<sup>1,2,\*</sup> and Ruxin Li<sup>2</sup>

<sup>1</sup>College of Science, University of Shanghai for Science and Technology, Shanghai 200093, People's Republic of China

<sup>2</sup>State Key Laboratory of High Field Laser Physics and CAS Center for Excellence in Ultra-Intense Laser Science, Shanghai Institute of Optics and Fine Mechanics (SIOM), Chinese Academy of Sciences (CAS), Shanghai 201800, China



(Received 19 October 2022; revised 11 January 2023; accepted 17 January 2023; published 10 February 2023)

We perform nonperturbative calculations of light-field driven valley-polarization process in monolayer MoS<sub>2</sub> which has additional Rashba spin-orbit couplings (SOCs). The ultrafast electron dynamics is simulated within the independent particle picture by solving density-matrix equations in the basis of linear combination of atomic orbitals, where tight-binding (TB) models including both intrinsic atomic and Rashba SOC are used to calculate relevant matrix elements. We demonstrate that the Rashba-type SOC can be manifested by suboptical-cycle control of valley selectivity excitations, in particular necessary via using few-cycle linearly polarized pulse with controlled carrier-envelope phase (CEP). This procedure will lead to a CEP-dependent valley Hall conductivity (VHC), which exhibits an important phase shift among different Rashba coupling strengths. The additional analysis shows that this phase shift is mainly determined by the  $d^2$ -orbital TB Rashba parameter from Mo atom and originates from contribution of conduction bands to VHC, where the Berry curvature modified by Rashba SOC plays a crucial role. Moreover, we also provide a qualitative interpretation on the Rashba-dependent VHC in terms of suboptical-cycle Landau-Zener-Stückelberg interference. Our results suggest a feasible approach for probing Rashba SOC in hexagonal two-dimensional materials, and might pave the way of achieving more controls in the future valleytronics application.

DOI: [10.1103/PhysRevResearch.5.013098](https://doi.org/10.1103/PhysRevResearch.5.013098)

### I. INTRODUCTION

The strong-field excitation of solids with ultrashort laser pulse is able to yield a great deal of complex ultrafast processes [1–3]; in particular, using the carrier wave of laser pulse to manipulate and steer multiple degrees of freedom of electrons in solids on the suboptical-cycle timescale forms the core of lightwave electronics [4,5]. It is aimed at both the fundamental investigation of rich solid-state ultrafast phenomena and the promising realization of application in high-speed signal processing at the optical frequency [6–8].

One of the important controls over electron transport is related with its valley pseudospin degree of freedom which widely exists in hexagonal two-dimensional (2D) materials with broken-inversion symmetry [9], such as monolayer transition-metal dichalcogenides (TMDs) of intensive concern by many theoretical and experimental studies [10–15]. In the 2D hexagonal lattices, valleys as the local extreme are located at  $K$  and  $K'$  points of the Brillouin zone. Recently, great efforts have been performed towards the ultrafast manipulation of valley selectivity excitation on the timescale faster than valley depolarization, crucial for valleytronic application [16]. This

has been successfully demonstrated by a series of methods based on the coherent optical control using hybrid laser pulses [17,18] or single linearly polarized few-cycle [19–21] pulses. The induced valley asymmetry in such 2D materials can be subsequently captured by measuring nonzero valley Hall conductivity (VHC) as a result of the opposite Berry curvatures at two inequivalent  $K$  valleys, intrinsically originating from the lattice in-plane broken-inversion symmetry [22].

When the inversion symmetry further breaks in the direction perpendicular to the 2D plane, generally achieved by placing the 2D material in an external electric field or on a polar substrate, the additional Rashba-type spin-orbit couplings (SOCs) naturally occur [23–25]. The most important characteristics of Rashba SOC refer to the odd dependence on the electron momentum, which can drive a wide variety of fascinating phenomena. Signatures of Rashba SOC are usually extracted by the analysis of Shubnikov–de Haas oscillations [26] and angle-resolved photoemission spectroscopy [27–29]. For the doping gate or polar TMDs, it is also predicted that Rashba SOC can be detected by Kerr effect experiments [30]. In the strong-field interaction regime, Rashba SOC still play an important role in some nonlinear process, such as high-order harmonic generation [31]. Despite this, the effect of Rashba SOC on the other strong-field ultrafast optical response of 2D systems has not yet been well explored.

In this work, we bring Rashba effect into the well-established concept of lightwave-driven subcycle dynamics of valley polarization in TMDs. Specifically, taking monolayer MoS<sub>2</sub> as an example, we demonstrate a scheme for observing signature of Rashba SOC that is introduced by the

\*cdliu@siom.ac.cn

Published by the American Physical Society under the terms of the [Creative Commons Attribution 4.0 International license](https://creativecommons.org/licenses/by/4.0/). Further distribution of this work must maintain attribution to the author(s) and the published article's title, journal citation, and DOI.

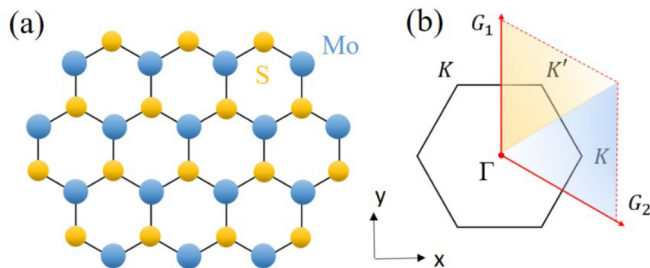


FIG. 1. (a) Top view of monolayer MoS<sub>2</sub> lattice, with each sublattice occupied by a Mo (blue) and two S (yellow) atoms. (b) First Brillouin zone in the reciprocal lattice.  $\mathbf{G}_1$  and  $\mathbf{G}_2$  are two reciprocal lattice primitive vectors.

external input. The method relies on valley-selective excitations of all-optical preparation realized by linearly polarized few-cycle pulse with stabilized carrier-envelope phase (CEP). It is expected that the resulting VHC accessible in experiments can encode the information on Rashba effects, since the additional Rashba SOC affects the whole electronic band structures and especially modify Berry curvature around valleys. To obtain the nonlinear ultrafast electronic dynamics in such Rashba system, we solve the length-gauge Liouville–von Neumann equation in the linear combination of atomic orbitals representation. Compared with the standard time-dependent Schrödinger equation, the Liouville–von Neumann equation can both automatically take into account Pauli blocking of interband transitions and phenomenologically include the relaxation process. The implementation of its parametrization is based on simplified six-band tight-binding (TB) models in which intrinsic spin-orbit splitting and external Rashba SOC are simultaneously included. Here, in contrast to the usual low-energy treatment of expanding Hamiltonian around some high-symmetry points, the complete MoS<sub>2</sub> electronic structures are employed to properly take into account that the movement of electrons under strong fields will extend to a larger region of Brillouin zone (BZ). We discuss the behavior of induced VHC upon observing its dependence on several laser and material parameters, with the particular emphasis on influence of Rashba coupling strengths. It is shown that the CEP-dependent VHC exhibits an important phase shift, whose value is determined by the magnitude of phenomenological Rashba parameter, thus suggesting a feasible approach to characterize Rashba effect. The underlying physical origin of this kind of Rashba-related phase shift is also successfully revealed. Moreover, we offer a qualitative interpretation in terms of the suboptical-cycle Landau-Zener-Stückelberg (LZS) interference picture.

## II. THEORETICAL MODLES

The atoms in monolayer MoS<sub>2</sub> lattice are arranged in trigonal prismatic fashion ( $P-6m2$  space group) where the unit cell consists of three atoms, i.e., Mo atom sandwiched between two S atoms [32]. The in-plane atomic structure is formed by alternating arrangement of Mo and S atom in a hexagonal honeycomb way similar to graphene, as shown in Fig. 1(a). Figure 1(b) shows the corresponding hexagonal BZ,

together with its parallelogram equivalent spanned by two reciprocal-lattice primitive vectors  $\mathbf{G}_1$  and  $\mathbf{G}_2$ . The latter is more convenient for sampling  $\mathbf{k}$  points and defining valley asymmetry of  $K$  and  $K'$ .

In the calculation, the electronic band structure of MoS<sub>2</sub> is described by the TB model in which SOC are only considered from the on-site contribution of heavy Mo atoms. Using the minimal set of Mo- $|d_{z^2}, \uparrow\rangle$ ,  $|d_{xy}, \uparrow\rangle$ ,  $|d_{x^2-y^2}, \uparrow\rangle$ ,  $|d_{z^2}, \downarrow\rangle$ ,  $|d_{xy}, \downarrow\rangle$ ,  $|d_{x^2-y^2}, \downarrow\rangle$  orbitals as basis, the full TB Hamiltonian that covers the external Rashba effect is given by [30,33–35]

$$H_{TB}(\mathbf{k}) = H_{TNN}(\mathbf{k}) \otimes I_2 + \frac{1}{2}\lambda L_z \otimes \sigma_z + H_c(\mathbf{k}) \otimes \sigma_z + H_R(\mathbf{k}), \quad (1)$$

where  $I_2$  is the  $2 \times 2$  identity matrix,  $H_{TNN}(\mathbf{k})$  is the spinless  $3 \times 3$  Hamiltonian matrix constructed under the  $D_{3h}$  symmetry and the third-nearest-neighbor Mo-Mo hoppings, the middle two terms represent intrinsic SOC, and the last term refers to Rashba SOC probably emerging from polar or gated MoS<sub>2</sub>. By the first-order perturbation analysis of Eq. (1), the second term can lead to spin-orbit splitting of  $\Delta_{SOC}^v = 2\lambda$  at the  $K$  ( $K'$ ) valley for valence band (VB) and keep the conduction band (CB) still degenerate. In contrast, the CB spin splitting is dominated by the third term of Eq. (1), known as Ising SOC [36,37]. Here, the Rashba SOC take the form of [30]

$$H_R(\mathbf{k}) = \begin{pmatrix} 2\alpha_0 & 0 & 0 \\ 0 & 2\alpha_2 & 0 \\ 0 & 0 & 2\alpha_2 \end{pmatrix} \otimes (f_x(\mathbf{k})\sigma_y - f_y(\mathbf{k})\sigma_x), \quad (2)$$

with TB parameters  $\alpha_0$  and  $\alpha_2$  corresponding to  $d_{z^2}$  and  $\{d_{xy}, d_{x^2-y^2}\}$  orbitals, respectively. On the other hand, Rashba effect is always phenomenologically written in a simple model Hamiltonian [38] for 2D electrons confined to the  $xy$  plane and subjected to an electric field along the  $z$  direction as  $H_R(\mathbf{k}) = \alpha_R(\boldsymbol{\sigma} \times \mathbf{k}) \cdot \hat{\mathbf{z}}$ , where  $\alpha_R$  denotes the Rashba coupling strength. Note that  $\alpha_0$  and  $\alpha_2$  shown in Eq. (2) are different from  $\alpha_R$ . By expanding the functions  $f_{x/y}(\mathbf{k})$  in Eq. (2) around  $K$  or  $K'$  valleys, it is easily seen that the Rashba coupling strength  $\alpha_c$  for CB and  $\alpha_v$  for VB can be related to  $\alpha_0$  and  $\alpha_2$  by  $\alpha_c = 2\alpha_0 a/3$  and  $\alpha_v = 2\alpha_2 a/3$ , where  $a$  is the lattice constant. In the following text, we use  $\alpha_c$  and  $\alpha_v$  to describe the magnitude of Rashba effect instead of the TB parameters  $\alpha_0$  and  $\alpha_2$ . Other detailed matrix elements and formulas required for the complete  $6 \times 6$  Hamiltonian matrix  $H_{TB}(\mathbf{k})$  can be found in Appendix A.

The strong-field interaction of MoS<sub>2</sub> with an ultrashort pulse can be modeled within independent particle approximation, which allows one to describe the system using one electron density operator. In the length gauge (LG) and within the dipole approximation, the temporal evolution of density operator  $\rho(t)$  is given by Liouville–von Neumann equation [39,40]

$$i \frac{d}{dt} \rho(t) = [H_0 + \mathbf{E}(t) \cdot \mathbf{r}, \rho(t)], \quad (3)$$

where  $H_0$  is the field-free Hamiltonian and  $\mathbf{E}(t)$  is the time-dependent electric field. Unless otherwise indicated, atomic units (a.u.) are used throughout:  $e = \hbar = m_e = 1$ , where  $e$  and  $m_e$  are the electron charge and mass, respectively. The LG

suggests us to solve Eq. (3) within a frame of crystal momentum moving with the vector potential  $\mathbf{A}(t) = -\int_{-\infty}^t \mathbf{E}(\tau) d\tau$ , since it is able to decouple the different  $\mathbf{k}$  and particularly convenient for numerical implementation. In this case, the reduced density operator for an initial crystal momentum  $\mathbf{k}_0$  can be expressed as

$$\rho^{\mathbf{k}_0}(t) = \sum_{i,j} \rho_{ij}^{\mathbf{k}_0}(t) |B_{i,\mathbf{k}(t)}\rangle \langle B_{j,\mathbf{k}(t)}|, \quad (4)$$

where  $B_{i,\mathbf{k}(t)}$  is the comoving basis function with the time-dependent momentum  $\mathbf{k}(t) = \mathbf{k}_0 + \mathbf{A}(t)$ , constructed by the Bloch sum of atomic orbital  $i$ . Here, we introduce a compound index  $i = \{n, \alpha\}$ , in which  $n$  labels a given atom in the unit cell and  $\alpha$  represents the orbital shape on this atom. If the field-free electronic structure is described by the TB Hamiltonian  $H_{TB}(\mathbf{k})$ , the resulting equation of motion for coefficients  $\rho_{ij}^{\mathbf{k}_0}(t)$  can be written in a matrix form of

$$i \frac{d}{dt} \rho^{\mathbf{k}_0}(t) = [H_{TB}(\mathbf{k}), \rho^{\mathbf{k}_0}(t)], \quad (5)$$

where  $\rho^{\mathbf{k}_0}(t)$  is the density matrix comprising the element  $\rho_{ij}^{\mathbf{k}_0}(t)$ . Hence, the temporal evolution of  $\rho^{\mathbf{k}_0}(t)$  is simply governed by a complete set of ordinary differential equations. The detailed derivation and some approximate conditions used for obtaining Eq. (5) are presented in Appendix B.

We point out that  $\rho^{\mathbf{k}_0}(t)$  denotes the density matrix in the presentation of atomic orbitals. For a clearer analysis of physical processes, it is helpful to express density operator in the valence- and conduction-band representation as

$$\rho^{\mathbf{k}_0}(t) = \sum_{i,j} \tilde{\rho}_{ij}^{\mathbf{k}_0}(t) |i, \mathbf{k}(t)\rangle \langle j, \mathbf{k}(t)|, \quad (6)$$

where  $|i, \mathbf{k}(t)\rangle$  represents the  $i$ th Bloch basis function that is the eigenstate of  $H_{TB}(\mathbf{k})$ . The coefficient  $\tilde{\rho}_{ij}^{\mathbf{k}_0}(t)$  therefore forms a density-matrix  $\tilde{\rho}^{\mathbf{k}_0}(t)$  in the band representation. It is easily seen that density matrix in two different representations is related by a unitary transformation:

$$\tilde{\rho}^{\mathbf{k}_0}(t) = \mathbf{U}_{\mathbf{k}(t)}^\dagger \rho^{\mathbf{k}_0}(t) \mathbf{U}_{\mathbf{k}(t)}, \quad (7)$$

and

$$\rho^{\mathbf{k}_0}(t) = \mathbf{U}_{\mathbf{k}(t)} \tilde{\rho}^{\mathbf{k}_0}(t) \mathbf{U}_{\mathbf{k}(t)}^\dagger, \quad (8)$$

where  $\mathbf{U}_{\mathbf{k}(t)}$  is a unitary matrix constructed by arranging the eigenvectors of  $H_{TB}(\mathbf{k})$  in columns. Thus, the diagonal element  $\tilde{\rho}_{ii}^{\mathbf{k}_0}(t)$  of  $\tilde{\rho}^{\mathbf{k}_0}(t)$  directly provides information on time-dependent population of electrons occupying the  $i$ th band at a fixed  $\mathbf{k}_0$ .

We take  $160 \times 160$   $\mathbf{k}_0$  points from the parallelogram region shown in Fig. 1(b), and numerically solve Eq. (5) for each independent  $\mathbf{k}_0$  by the classical fourth-order Runge-Kutta method. For the ultrafast nonlinear process, decoherence arising from electron-electron scattering beyond the mean-field approximation needs proper consideration, which is typically on a few of femtoseconds timescale. This is usually treated by phenomenologically introducing a constant dephasing time  $T_2$  into the dynamical equation. We choose  $T_2 = 5$  fs, comparable to the value usually employed in the strong-field

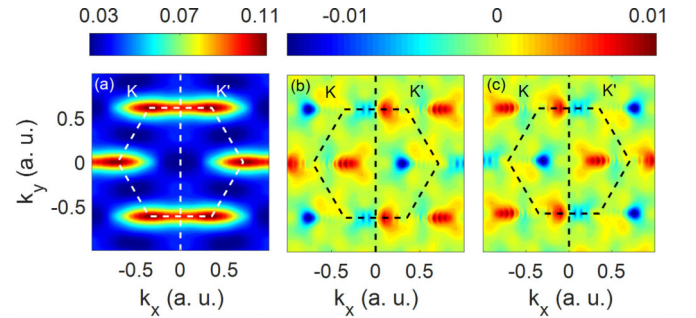


FIG. 2. Total CB population distribution in the reciprocal space after the interaction with driving pulses with CEP (a)  $\phi_{\text{CEP}} = 0$ , (b)  $\phi_{\text{CEP}} = \pi/2$ , and (c)  $\phi_{\text{CEP}} = 3\pi/2$ . For  $\phi_{\text{CEP}} = \pi/2$  and  $\phi_{\text{CEP}} = 3\pi/2$ , the population distribution is plotted by the difference compared with panel (a). The driving light has a Gaussian envelope with the central wavelength  $\lambda = 8 \mu\text{m}$ , duration 27 fs, and the peak intensity  $I_0 = 0.3 \text{ TW}/\text{cm}^2$ . The dashed hexagon represents the first BZ, and the vertical dashed line guides the eyes to observe the population asymmetry between  $K$  and  $K'$  valleys.

process such as high-harmonic generation [41]. However, the relaxation term cannot be directly added to Eq. (5), due to the fact that the dephasing process describes the exponential decay of interband polarization between bands and thus must impact on off-diagonal elements of  $\tilde{\rho}^{\mathbf{k}_0}(t)$  rather than  $\rho^{\mathbf{k}_0}(t)$ . Instead, we consider dephasing mechanism as follows: At each evolution step of solving Eq. (5) with the time interval  $\Delta t$ ,  $\rho^{\mathbf{k}_0}(t)$  is transformed to  $\tilde{\rho}^{\mathbf{k}_0}(t)$  via Eq. (7), followed by multiplying the off-diagonal element  $\tilde{\rho}_{ij}^{\mathbf{k}_0}(t)$  by  $\exp(-\Delta t/T_2)$ , and finally transformed back to  $\rho^{\mathbf{k}_0}(t)$  via Eq. (8). Repeat the above procedure until the end of dynamics evolution.

### III. RESULTS AND DISCUSSION

#### A. Phase shift of CEP-dependent VHC due to Rashba SOCs

In the strong-field regime, electron dynamics in  $\text{MoS}_2$  driven by few-cycle laser pulses exhibits an important dependence on the exact shape of optical carrier field [5,42–44], so that it is possible to control the electron population between valleys on a subcycle timescale by varying the CEP of driving pulse. In order to reveal the essentials of valley polarization and highlight its influence on capturing the Rashba effect, a single-cycle pulse with the linear polarization along the  $\Gamma-K$  direction is employed to achieve optical preparation of selective valley excitation.

We first observe the result for a 27-fs-long wavelength  $\lambda = 8 \mu\text{m}$  Gaussian pulse with a moderate peak intensity of  $I_0 = 0.3 \text{ TW}/\text{cm}^2$ , below the damage threshold [14]. At the end of the pulse  $t = t_f$ , the residual  $\mathbf{k}$ -resolved distribution of total CB population can be extracted by summing electron population in all of the CBs, defined as  $\tilde{\rho}_c(\mathbf{k}_0) = \sum_{i \in \text{CBs}} \tilde{\rho}_{ii}^{\mathbf{k}_0}(t_f)$ . Figure 2 shows the calculation result of  $\tilde{\rho}_c(\mathbf{k}_0)$  for three different CEP values: (a)  $\phi_{\text{CEP}} = 0$ , (b)  $\phi_{\text{CEP}} = \pi/2$ , and (c)  $\phi_{\text{CEP}} = 3\pi/2$ . One can see that for  $\phi_{\text{CEP}} = 0$  the driving pulse couples equally to both valleys, leading to the population distribution of mirror symmetry about  $\Gamma-M$  direction, while for  $\phi_{\text{CEP}} = \pi/2$  and  $\phi_{\text{CEP}} = 3\pi/2$  the asymmetry in the CB population of  $K$  and  $K'$  valleys is presented. Note that for  $\phi_{\text{CEP}} = \pi/2$

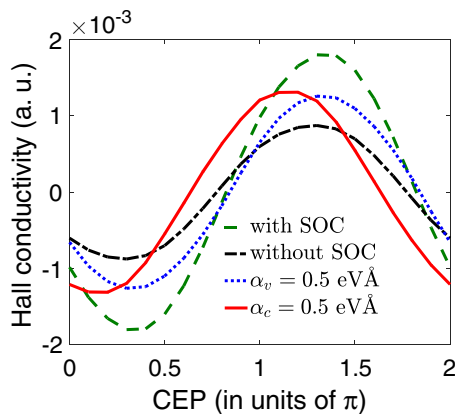


FIG. 3. Comparison of Hall conductivity calculated as a function of CEP for four different Hamiltonian systems: the intrinsic SOC Hamiltonian (green dashed), spinless Hamiltonian (black-dashed-dotted), and full Hamiltonian with  $\alpha_v = 0.5 \text{ eV \AA}$  and  $\alpha_c = 0$  (blue dotted), together with  $\alpha_v = 0$  and  $\alpha_c = 0.5 \text{ eV \AA}$  (red-solid). The laser parameters are the same as Fig. 2.

and  $\phi_{\text{CEP}} = 3\pi/2$ , the population distribution has been plotted by the difference compared with the  $\phi_{\text{CEP}} = 0$  case in order to highlight the discrepancy in the valley population. The comparison in Figs. 2(a)–2(c) clearly verifies the feasibility of selection valley polarization controlled by CEP, which can be simply attributed to the fact that for few-cycle driving pulse the vector potential value at the peak position of electric field varies with CEP [19]. Our calculations also show that different Rashba coupling strength  $\alpha_c$  and  $\alpha_v$  has less affected the CEP-dependent population distribution  $\tilde{\rho}_c(\mathbf{k}_0)$ . Thus, it is insufficient to manifest the Rashba SOC's imposed to MoS<sub>2</sub> by only observing  $\mathbf{k}$ -resolved population information.

On the other hand, the CEP-induced unequal valley population can lead to an observable valley Hall effect when an in-plane electric field is applied to MoS<sub>2</sub>, due to the opposite Berry curvatures at the  $K$  and  $K'$  valleys [45,46]. Once the valley population distribution forms, the measurement of generated current orthogonal to the applied electric field can give a CEP-dependent VHC as [47]

$$\sigma_{xy}(\phi_{\text{CEP}}) = -\frac{1}{(2\pi)^2} \sum_n \int_{\text{BZ}} d\mathbf{k}_0 \tilde{\rho}_{nm}^{\mathbf{k}_0}(t_f) \Omega_n(\mathbf{k}_0), \quad (9)$$

where  $\tilde{\rho}_{nm}^{\mathbf{k}_0}$  and  $\Omega_n(\mathbf{k}_0)$  are residual  $\mathbf{k}$ -resolved population and field-free Berry curvature of the  $n$ th band, respectively, and the sum runs over all VBs and CBs.

Figure 3 shows  $\sigma_{xy}$  as a function of CEP, calculated for four different cases, i.e., considering the intrinsic SOC Hamiltonian (green-dashed line) described by the first three terms of Eq. (1): spinless Hamiltonian  $H_{\text{TNN}}(\mathbf{k})$  (black-dashed-dotted line) without any SOC, full Hamiltonian  $H_{\text{TB}}(\mathbf{k})$  with  $\alpha_v = 0.5 \text{ eV \AA}$  and  $\alpha_c = 0$  (blue-dotted line), and full Hamiltonian  $H_{\text{TB}}(\mathbf{k})$  with  $\alpha_v = 0$  and  $\alpha_c = 0.5 \text{ eV \AA}$  (red solid line). In Fig. 3, the CEP-dependent  $\sigma_{xy}$  for the four cases all exhibit sine oscillations, with the phase determined by the specific Hamiltonian, where the Rashba SOC's through the parameter  $\alpha_c$  can generate a significant phase shift compared with the other three cases. In other words,  $d_z^2$ -orbital TB Rashba

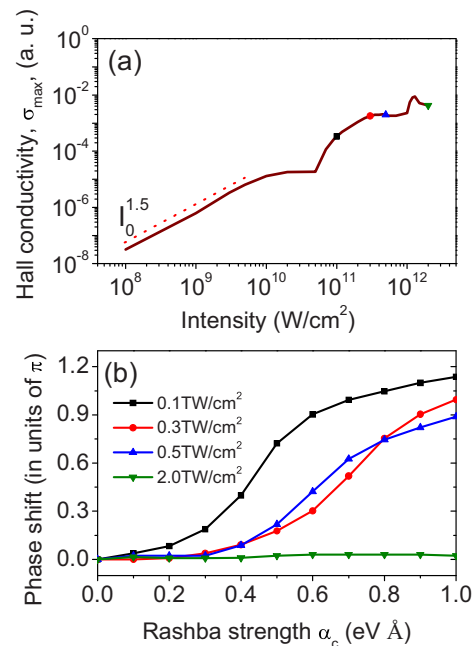


FIG. 4. (a) Maximum conductivity  $\sigma_{\text{max}}$  vs the laser intensity at a fixed  $\alpha_c = 0.5 \text{ eV \AA}$ . (b) Phase shift  $\delta(\alpha_c)$  as a function of  $\alpha_c$ , calculated from driving pulses with peak intensity  $I_0 = 0.1 \text{ TW/cm}^2$  (black squares),  $I_0 = 0.3 \text{ TW/cm}^2$  (red circles),  $I_0 = 0.5 \text{ TW/cm}^2$  (blue-up triangle), and  $I_0 = 2.0 \text{ TW/cm}^2$  (green-down triangle). Four symbols on the curve of panel (a) denote the selected intensity position corresponding to panel (b). The other laser parameters are the same as Fig. 2.

parameter from Mo atom dominates the phase shift. This is an evident observable for extracting the Rashba effect in the experiment. Therefore, we mainly focus on the  $\alpha_c$  influence on the CEP-dependent VHC in the following text.

In order to quantitatively estimate the phase shift induced by Rashba SOC's, we perform the curve fitting of the simulated  $\sigma_{xy}$  with the function form  $x_1 \sin[\phi_{\text{CEP}} + x_2(\alpha_c)]$ , where the fitting parameter  $x_2(\alpha_c)$  gives the phase for a given Rashba coupling strength  $\alpha_c$ . The phase shift due to the Rashba effect can be defined as  $\delta(\alpha_c) = x_2(\alpha_c) - x_2(\alpha_c = 0)$ . We plot  $\delta(\alpha_c)$  with changing  $\alpha_c$  in the case of four different driving-pulse peak intensities:  $I_0 = 0.1 \text{ TW/cm}^2$  (black squares),  $I_0 = 0.3 \text{ TW/cm}^2$  (red circles),  $I_0 = 0.5 \text{ TW/cm}^2$  (blue up-triangle), and  $I_0 = 2.0 \text{ TW/cm}^2$  (green down-triangle), as shown in Fig. 4(b). One can see that for moderate intensity ( $0.1 \sim 0.5 \text{ TW/cm}^2$ ) the phase shift increases monotonically with  $\alpha_c$  ranging from 0 to  $1.0 \text{ eV \AA}$ , during which the curve varies smoothly at both sides and rises rapidly in the middle region. Particularly at the relatively low intensity, phase shifts become more sensitive to  $\alpha_c$ , beneficial for observation of Rashba effect. On the contrary, when the pulse intensity reaches as high as  $I_0 = 2.0 \text{ TW/cm}^2$ , the phase shift is hardly affected by Rashba SOC's, thus preventing the possible application to Rashba detection. The laser intensity can also change the maximum magnitude of VHC, which nontrivially depends on CEP and might determine the accuracy of experimental measurement. At a fixed  $\alpha_c = 0.5 \text{ eV \AA}$ , we extract the maximum conductivity  $\sigma_{\text{max}}$  from the CEP-dependent  $\sigma_{xy}$  curve

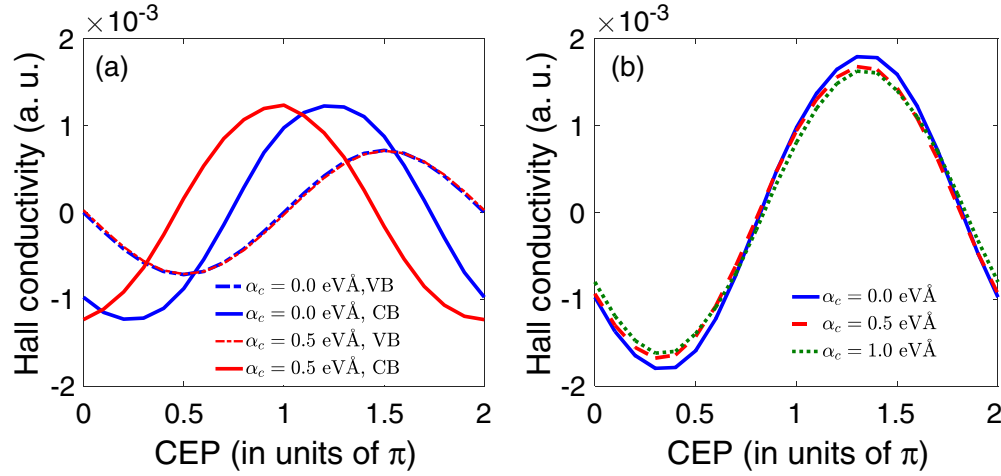


FIG. 5. (a) Comparison of different CEP-dependent Hall conductivity, obtained from VB contribution at  $\alpha_c = 0$  (blue dashed), from CB contribution at  $\alpha_c = 0$  (blue solid), from VB contribution at  $\alpha_c = 0.5$  eV Å, and from CB contribution at  $\alpha_c = 0.5$  eV Å. (b) CEP-dependent Hall conductivity calculated at  $\alpha_c = 0.0$  eV Å (blue solid),  $\alpha_c = 0.5$  eV Å (red-dashed), and  $\alpha_c = 1.0$  eV Å (green dot). For the three cases, Berry curvature is always chosen as the unmodified one corresponding to  $\alpha_c = 0.0$  eV Å. The laser parameters are the same as Fig. 2.

and observe its dependence on the intensity  $I_0$ . The result is reported in Fig. 4(a). We find that when the intensity is weak ( $I_0 < 10^{10}$  W/cm<sup>2</sup>), a typical power-law  $\sigma_{\max} \propto I_0^{1.5}$  is exhibited. This characteristic reflects the perturbative light-matter interaction. As the intensity increases, the power-law dependence of  $\sigma_{\max}$  on  $I_0$  breaks down, representing that electron dynamics gradually enter into the nonperturbative strong-field regime. For clarity, positions of maximum Hall conductivity corresponding to four intensities used in Fig. 4(b) have been marked in Fig. 4(a) with the same symbol. In the practical implement, the proper choice of laser intensity to observe Rashba effects should carefully take into account the balance of the  $\alpha_c$  sensitivity and the sufficiently strong Hall current signal.

### B. Origin of phase shift

Decomposition of VHC is helpful to identify the origin of this kind of phase shift. The summation in Eq. (9) can be divided into two parts according to whether  $n$  belong to VBs or CBs, naturally resulting in  $\sigma_{xy} = \sigma_{VB} + \sigma_{CB}$ , where  $\sigma_{VB}$  and  $\sigma_{CB}$  describe the VHC contribution from VBs and CBs, respectively. For the separated  $\sigma_{VB}$  and  $\sigma_{CB}$ , we compare their CEP-dependent behavior in the case of with Rashba SOCs ( $\alpha_c = 0.5$  eV Å) and without Rashba SOCs ( $\alpha_c = 0$ ), as given in Fig. 5(a). One can see that the Rashba SOCs cannot generate any phase shift for  $\sigma_{VB}$ , while an obvious phase shift occurs for  $\sigma_{CB}$  under different Rashba coupling strengths. Consequently, we can conclude that the phase shift of VHC induced by Rashba effects mainly originates from the CB contribution.

We now turn to the simple discussion of the effect of Berry curvature on phase shift. The Berry curvature that contributes to VHC through Eq. (9) can be efficiently controlled by the external Rashba SOCs. This relationship can be intuitively seen by analyzing an effective Hamiltonian near the CB  $K$  valleys, which is constructed under the basis formed by

Mo- $\{|d_{z^2}, \uparrow\rangle, |d_{z^2}, \downarrow\rangle\}$  orbitals and given by [37]

$$H_{\text{spin}}^c(\mathbf{k} + \varepsilon\mathbf{K}) = \left( \frac{|\mathbf{k}|^2}{2m_c^*} - \mu \right) \sigma_0 + \alpha_c (\boldsymbol{\sigma} \times \mathbf{k}) \cdot \hat{\mathbf{z}} + \varepsilon \beta_c \sigma_z, \quad (10)$$

where  $\mu$  is the chemical potential,  $m_c^*$  is the effective mass of the CB electron,  $\mathbf{k}$  is the crystal momentum measured relative to  $K$  valleys described by the index  $\varepsilon = \pm 1$ , and the last  $\beta_c$  term refers to the Ising SOC. From Eq. (10), the corresponding Berry curvature in the lower-spin bands can be expressed as

$$\Omega_{\text{spin}}(\mathbf{k} + \varepsilon\mathbf{K}) = \frac{\alpha_c^2 \varepsilon \beta_c}{2[(\alpha_c k)^2 + \beta_c^2]^{3/2}}. \quad (11)$$

Although Eq. (11) is a simple and approximate formula only valid around valleys, it clearly implies that Rashba SOCs can significantly change  $\mathbf{k}$ -resolved Berry curvature throughout the whole BZ. The importance of modified Berry curvature in generating the phase shift can be revealed by Fig. 5(b), where we have calculated the CEP-dependent VHC with Eq. (9) for three different Rashba coupling strengths:  $\alpha_c = 0.0$  eV Å (blue solid),  $\alpha_c = 0.5$  eV Å (red dashed), and  $\alpha_c = 1.0$  eV Å (green dot), under the condition that  $\Omega_n(\mathbf{k}_0)$  are always kept unchanged and set to the one of  $\alpha_c = 0.0$  eV Å. In this case, the phase shift is absent, representing the crucial role of Rashba-controlled Berry curvatures.

Another factor that affects VHC is related with the residual population in the  $\mathbf{k}$  space as described by Eq. (9). The final electron distribution is strongly dependent on the light-induced excitation process. When the carrier frequency of pulses is well below the band gap of MoS<sub>2</sub>, electron dynamics can be described by Landau-Zener (LZ) transitions. In this regime, the electron injection into the conduction band mainly occurs when it passes near the valleys. For our used linearly polarized pulse, the oscillatory electric field can drive electrons to pass near the band-gap minimum repeatedly within one optical cycle. This may form different excitation quantum pathways per cycle, leading to the so-called

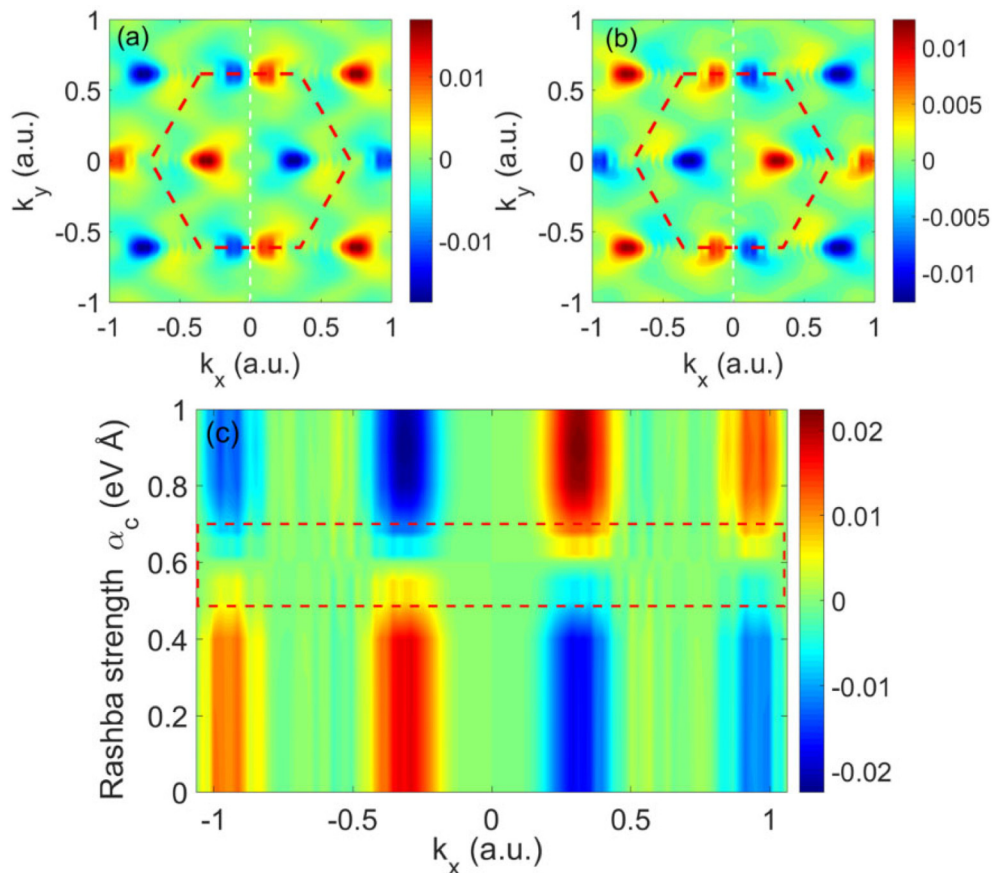


FIG. 6. (a), (b) The  $\mathbf{k}$ -resolved difference  $\Delta\rho_c(\mathbf{k}_0)$  between the residual CBs population resulting from excitation with a pair of CEP  $\phi_1$  and  $\phi_2$ , calculated at two different Rashba coupling strength (a)  $\alpha_c = 0.3$  eV Å and (b)  $\alpha_c = 0.7$  eV Å. (c) Extracted  $\Delta\rho_c(\mathbf{k}_0)$  along  $k_y = 0$  changing with  $\alpha_c$ . The red-dashed rectangle represents the transition region across which the sign of  $\Delta\rho_c(\mathbf{k}_0)$  reverses. The laser parameters are the same as Fig. 2.

intracycle LZS interference [48], which plays an important role in the strong-field process [5,49]. The phase relationship among these pathways determines the final momentum-dependent CB population. It is well known that this phase depends on not only light waveform but also electronic band structures. Especially, the latter can be further affected by the Rashba SOCs, which results in Rashba-controlled population distribution and in turn is responsible for the phase shift involved in the CEP-dependent VHC.

In order to clearly track how Rashba SOCs change the  $\mathbf{k}$ -resolved CB distribution, we introduce  $\Delta\rho_c(\mathbf{k}_0)$ , obtained by the difference between residual CB population after using excitation pulses with two different CEPs,  $\phi_1$  and  $\phi_2$ . The  $\phi_1$  and  $\phi_2$  differ by  $\pi$  and correspond, respectively, to the minimum and maximum position in the CEP-dependent VHC. At  $\alpha_c = 0.3$  eV Å, we plot  $\Delta\rho_c(\mathbf{k}_0)$  in Fig. 6(a), where the red and blue spot regions show a clear CEP difference, antisymmetrically in the  $k_x$  direction. For comparison, we increase the Rashba strength to  $\alpha_c = 0.7$  eV Å, which yields  $\Delta\rho_c(\mathbf{k}_0)$  in Fig. 6(b). In this case, the sign of all spot areas have reversed, thus giving direct evidence for the control of the  $\mathbf{k}$ -resolved CB distribution by Rashba SOCs.

It is worth pointing out that the strongest signal (difference) in Fig. 6(a) and Fig. 6(b) is not at  $K$  ( $K'$ ) points, which can be qualitatively interpreted as follows: For the driving pulse with

the photon energy smaller than the band gap, the electron is mainly launched at  $K$  or  $K'$  points via Landau-Zener transition mechanism. In this case, the CB population at  $K$  ( $K'$ ) points is mainly determined by the wavelength and the intensity of driving light, rather than the exact pulse waveform controlled by CEP. However, for the population at position far from CB minimum, the electron needs to undergo transport from valley position, which is now strongly dependent on the pulse waveform controlled by CEP. Hence, the strongest signal (due to CEP difference) is not at  $K$  ( $K'$ ) points. On the other hand, we have examined that the strongest specific position exhibits a dependence on the driving pulse wavelength. Indeed, an additional simulation for using 4-um driving pulse demonstrates that the strongest signal is still not at  $K$  ( $K'$ ) points and a shift takes place.

We next extract  $\Delta\rho_c(\mathbf{k}_0)$  along a fixed line  $k_y = 0$  and observe its variation with  $\alpha_c$ . The result is reported in Fig. 6(c), in which the two dashed horizontal lines at about  $\alpha_c = 0.5$  eV Å and  $\alpha_c = 0.7$  eV Å represent the position where  $\Delta\rho_c(\mathbf{k}_0)$  changes abruptly. Along the vertical axis, a significant change in the sign of  $\Delta\rho_c(\mathbf{k}_0)$  occurs when going across the transition area formed between the two dashed lines. It is worth pointing out that the transition area matches well with the region of rapid increase of phase shift  $\delta(\alpha_c)$  [see Fig. 4(b)].

### C. Interpretation in terms of LZS interference

The qualitative insight into the time evolution of CB population governed by LZS interference can be additionally obtained by writing the relevant phase analytically. There are two phases related with LZS interference. One is the transition phase of single LZ process, known as Stokes phase, and the other is the propagation phase. We only focus on the latter, since it mainly determines the residual CB distribution, and is given by [48,50]

$$\varphi_{CV} = \int_{t_1}^{t_2} [E_C(\mathbf{k}(\tau)) - E_V(\mathbf{k}(\tau))] d\tau, \quad (12)$$

where  $t_1$  and  $t_2$  refer to two LZ transition events in the same optical cycle. Here, the energy spectra  $E_C(\mathbf{k})$  for the lower-spin subbands near the CB minimum is obtained from eigenvalues of the Hamiltonian Eq. (10), and simultaneously VB dispersion  $E_V(\mathbf{k})$  near  $K$  valleys is approximated as the parabolic form. As a result, we can express  $\varphi_{CV}$  as

$$\varphi_{CV} = \int_{t_1}^{t_2} \left\{ E_g + \frac{[\mathbf{k}_0 + \mathbf{A}(\tau) - \varepsilon \mathbf{K}]^2}{2\mu} - \sqrt{\alpha_c^2 [\mathbf{k}_0 + \mathbf{A}(\tau) - \varepsilon \mathbf{K}]^2 + (\varepsilon \beta_c)^2} \right\} d\tau, \quad (13)$$

where  $E_g$  is the band gap and  $\mu$  is the reduced electron-hole effective mass. We simply assume the initial wave vector  $\mathbf{k}_0$  fixed at  $K$  valleys, and the vector potential has the form  $\mathbf{A}(\tau) = \sqrt{I_0} \omega_0^{-1} g(\tau) \sin(\omega_0 \tau + \phi_{\text{CEP}})$ , where  $g(\tau)$  is pulse envelope. Considering rather small  $\beta_c$ , one can rewrite Eq. (13) in the form of

$$\varphi_{CV} \approx C_0 + I_0 C_1 + \alpha_c \sqrt{I_0} C_2, \quad (14)$$

where  $C_0$ ,  $C_1$ , and  $C_2$  are some constants. The  $\varphi_{CV}$  shows that the Rashba strength  $\alpha_c$  can control the propagation phase, thus affecting the CB population and eventually leading to the phase shift of CEP-dependent VHC. We also note that for the high-intensity  $I_0$  the second term in Eq. (14) will contribute more to  $\varphi_{CV}$  than the last term, so that the phase shift  $\delta(\alpha_c)$  becomes insensitive to  $\alpha_c$ . This interpretation is consistent with the simulation results [see green-down triangle line in Fig. 4(b)].

The physical picture that intracycle LZS interference enables to generate the  $\alpha_c$ -dependent phase shift can be further supported by comparing simulation results using other driving light waveform. In contrast to few-cycle light-driven one-dimensional electron trajectory, we explore the 2D electron motion steered by counter-rotating bicircular (CRB) light field, consisting of a fundamental circularly polarized pulse (8000 nm, 0.12 TW/cm<sup>2</sup>) and its counter-rotating second harmonics (4000 nm, 0.03 TW/cm<sup>2</sup>). The pulse duration of CRB field is set as 27 fs. It has been demonstrated that the CRB light field can manipulate the subcycle valley transport dynamics by controlling the relative phase  $\Delta\varphi$  between two colors [17]. For describing valley selection excitation, we define the valley population asymmetry as  $A = 2(\tilde{\rho}_c^{\mathbf{K}} - \tilde{\rho}_c^{\mathbf{K}'}) / (\tilde{\rho}_c^{\mathbf{K}} + \tilde{\rho}_c^{\mathbf{K}'})$ , where  $\tilde{\rho}_c^{\mathbf{K}}$  and  $\tilde{\rho}_c^{\mathbf{K}'}$  are obtained by integrating the residual CB population over the colored-triangle region centered at  $K$  ( $K'$ ) in Fig. 1(b).

As expected, our calculations show that the  $\Delta\varphi$  can control valley population asymmetry in the same behavior for two different Rashba strengths,  $\alpha_c = 0$  (red solid) and  $\alpha_c = 0.5$  eV Å (blue dashed), as plotted in Fig. 7(b). For both cases, Fig. 7(c) shows the corresponding VHC as a function of  $\Delta\varphi$ . Although they exhibit sine oscillations similar to Fig. 3, the phase shift between them is absent. The difference can be understood by electron trajectories resulting from CRB field, as illustrated in Fig. 7(a). For this kind of trajectory, only one LZ transition per optical cycle is most likely to occur, since the electron passes near  $K$  valleys only once per cycle, which contributes to the maximal transition probability. Therefore, the intraoptical-cycle LZS interference condition does not meet, so that the phase shift of VHC due to Rashba SOC disappears.

Besides, we also consider the superposition of a near-infrared resonant pulse (5 fs/800 nm), which predominately populates both valleys of MoS<sub>2</sub>, and a long-wavelength control pulse (27 fs/8000 nm), which determines the electron transport property between  $K$  and  $K'$  valleys. Both pulses with the same intensity  $I_0 = 0.1$  TW/cm<sup>2</sup> are linearly polarized along the  $\Gamma-K$  direction, and their temporal delay is fixed at  $t_d = 0$ . We have demonstrated that changing CEP of the control pulse can achieve the selective valley excitation. The result is reported in Fig. 7(d), which shows the valley population asymmetry as a function of CEP, calculated for two different Rashba strength,  $\alpha_c = 0$  (red solid) and  $\alpha_c = 0.5$  eV Å (blue dashed). Since the electron excitation is mainly determined by the resonant pulse, whose photon energy matches with the band gap and duration is much shorter than the optical cycle of control pulse, the resulting single-photon transition can be considered as instantaneous process. Evidently, there is only one transition event in the case of two-color combined field, thus preventing LZS interference. It is expected that the phase shift of VHC cannot occur. Indeed, our simulation confirms the prediction when the VHC is calculated as a function of CEP of control pulses, given in Fig. 7(e). One can see that the oscillation still appears, while the phase shift between the two curves is absent. Therefore, the above simulations demonstrate that the intraoptical-cycle LZS interference plays an important role in the  $\alpha_c$ -dependent phase shift.

### D. Prospect of possible experimental devices in the future

In order to illustrate the scheme of probing Rashba effect discussed in this work, we propose a schematics for the possible implementation in the future nanodevice, as shown in Fig. 8. Monolayer MoS<sub>2</sub> sample of a few micrometers in size is used as active medium and transferred onto a substrate. An additional vertical gating electric field is applied to control the Rashba coupling strength of the MoS<sub>2</sub> regime. The gating field can be achieved by preparing an electrode placed on the monolayer surface using the material such as graphene or doped Si, which could provide an excellent optical transmittance for the excitation pulse at a wide range of midinfrared wavelength (e.g., 2–8  $\mu\text{m}$ ). The Hall effect is then probed by two pairs of electrodes placed at both sides of sample, as denoted by A and B in Fig. 8. The in-plane probe electric field can be provided by the electrode pair A, which drives an orthogonal current, followed by measuring the transverse

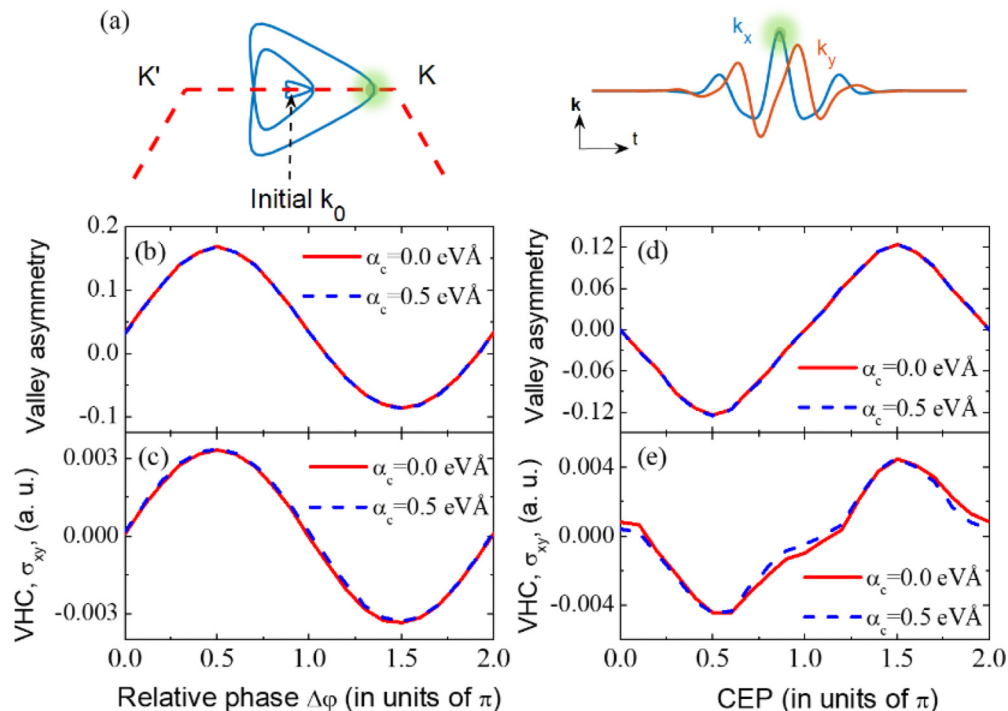


FIG. 7. (a) Two-dimensional electron trajectories in  $k$  space for CRB driving field. The electron starts from the initial  $\mathbf{k}_0$ , and the transition probability reaches the maximum (green-shaded circles) when electron passes near the  $K$  valley. The electron undergoes excitation with large transition probabilities only once per optical cycle. (b), (d) Valley population asymmetry as a function of (b) two-color relative phase  $\Delta\varphi$  for the CRB field, and (d) CEP of control pulse for the two linearly polarized superposition fields, calculated at  $\alpha_c = 0.0$  eV Å (red solid) and  $\alpha_c = 0.5$  eV Å (blue dashed). (c), (e) VHC  $\sigma_{xy}$  as a function of (c) two-color relative phase  $\Delta\varphi$  for the CRB field, and (e) CEP of control pulse for the two linearly polarized superposition fields, calculated at  $\alpha_c = 0.0$  eV Å (red solid) and  $\alpha_c = 0.5$  eV Å (blue dashed).

Hall voltage with the electrode pair  $B$  to estimate the Hall conductivity.

As for driving laser parameters, they do not sensitively affect the conclusion in this work. We have examined a series of driving wavelengths ranging from 4 to 8  $\mu\text{m}$ . It is found that the phase shift in the CEP-dependent Hall conductivity always exists among different Rashba SOCs strengths, except that the quantitative phase shift slightly depends on the wavelength. It is preferable to use the few-cycle-long wavelength pulse as the excitation light, since this kind of laser parameters enables to drive efficiently the electron transport between  $K$  and  $K'$  valleys in such a manner that the selection valley excitation

can take place. Hence, the valley Hall conductivity can be obtained for probing Rashba effect.

For the Hamiltonian model Eq. (1), the Rashba coupling strength is described by the coefficient  $\alpha_v$  and  $\alpha_c$ . They are difficult to be directly related with the gating field. In order to explicitly give how the gating field controls the Rashba effect and subsequently affects the phase shift in the CEP-dependent Hall conductivity, we consider a different tight-binding model where the vertical gating field is included. The detailed description and result can be found in Appendix C.

#### IV. CONCLUSIONS

In summary, we have theoretically investigated the nonlinear optical response of monolayer  $\text{MoS}_2$  having an additional Rashba SOCs to the intense few-cycle linearly polarized pulse. The strong-field electron dynamics is simulated by single-particle density-matrix equation, which is constructed by the linear combination of atomic orbitals within the tight-binding approximation framework.

We demonstrate that the lightwave-induced ultrafast dynamics of valley electron transport leads to an observable valley Hall effect, which enables to manifest the Rashba SOCs through leaving a distinct fingerprint into the VHC when scanning CEP. It is found that the phase shift of CEP-dependent VHC encodes the information on Rashba coupling strength, thus suggesting an approach to probe Rashba effects.

We successfully identify that the phase shift originates from the CB contribution and is mainly related to the  $d_z^2$ -

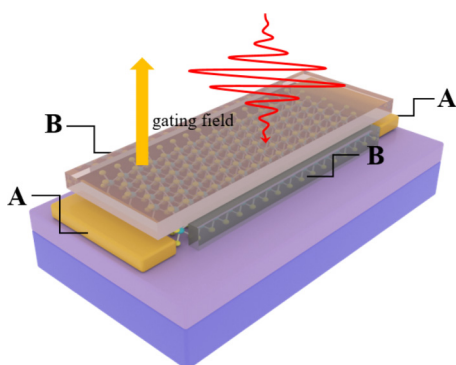


FIG. 8. Schematics of the device for probing Rashba effect.

orbital TB Rashba parameter from Mo atom. The joint effect of both Berry curvature and CB population distribution modified by Rashba SOCs is responsible for forming the phase shift. In particular, the  $\mathbf{k}$ -resolved residual CBs population is analyzed, which reveals an important signature of Rashba-controlled CB distribution. Accordingly, we provide an interpretation for the phase shift in terms of LZS interference. The physical picture is further supported by comparing with other optical preparation schemes of valley polarization in which the intracycle LZS interference hardly take place. Our work reveals optical and electric properties controlled by Rashba SOCs in the hexagonal 2D materials, which might be used in future valleytronics.

### ACKNOWLEDGMENTS

This work was supported by the National Natural Science Foundation of China (Grants No. 12174413 and No. 61690223), and the Strategic Priority Research Program of the Chinese Academy of Sciences (Grant No. XDB16).

### APPENDIX A: TIGHT-BINDING HAMILTONIAN

In this appendix we provide the explicit expression for calculating the full TB Hamiltonian  $H_{TB}(\mathbf{k})$ . In Eq. (1), the three-band TNN Hamiltonian is written as [33]

$$H_{TNN}(\mathbf{k}) = \begin{pmatrix} V_0 & V_1 & V_2 \\ V_1^* & V_{11} & V_{12} \\ V_2^* & V_{12}^* & V_{22} \end{pmatrix}, \quad (\text{A1})$$

where

$$\begin{aligned} V_0 &= \varepsilon_1 + 2t_0(2 \cos \alpha \cos \beta + \cos 2\alpha) \\ &+ 2r_0(2 \cos 3\alpha \cos \beta + \cos 2\beta) \\ &+ 2\mu_0(2 \cos 2\alpha \cos 2\beta + \cos 4\alpha), \end{aligned} \quad (\text{A2})$$

$$\begin{aligned} \text{Re}[V_1] &= -2\sqrt{3}t_2 \sin \alpha \sin \beta + 2(r_1 + r_2) \sin 3\alpha \sin \beta \\ &- 2\sqrt{3}\mu_2 \sin 2\alpha \sin 2\beta, \end{aligned} \quad (\text{A3})$$

$$\begin{aligned} \text{Im}[V_1] &= 2t_1 \sin \alpha (2 \cos \alpha + \cos \beta) + 2(r_1 - r_2) \\ &\times \sin 3\alpha \cos \beta + 2\mu_1 \sin 2\alpha (2 \cos 2\alpha + \cos 2\beta), \end{aligned} \quad (\text{A4})$$

$$\begin{aligned} \text{Re}[V_2] &= 2t_2(\cos 2\alpha - \cos \alpha \cos \beta) \\ &- \frac{2}{\sqrt{3}}(r_1 + r_2)(\cos 3\alpha \cos \beta - \cos 2\beta) \\ &+ 2\mu_2(\cos 4\alpha - \cos 2\alpha \cos 2\beta), \end{aligned} \quad (\text{A5})$$

$$\begin{aligned} \text{Im}[V_2] &= 2\sqrt{3}t_1 \cos \alpha \sin \beta + \frac{2}{\sqrt{3}} \sin \beta (r_1 - r_2) \\ &\times (\cos 3\alpha + 2 \cos \beta) \\ &+ 2\sqrt{3}\mu_1 \cos 2\alpha \sin 2\beta, \end{aligned} \quad (\text{A6})$$

$$\begin{aligned} V_{11} &= \varepsilon_2 + (t_{11} + 3t_{22}) \cos \alpha \cos \beta + 2t_{11} \\ &\times \cos \alpha + 4r_{11} \cos 3\alpha \cos \beta \\ &+ 2(r_{11} + \sqrt{3}r_{12}) \cos 2\beta + (u_{11} + 3u_{22}) \\ &\times \cos 2\alpha \cos 2\beta + 2u_{11} \cos 4\alpha, \end{aligned} \quad (\text{A7})$$

$$\begin{aligned} \text{Re}[V_{12}] &= \sqrt{3}(t_{22} - t_{11}) \sin \alpha \sin \beta + 4r_{12} \sin 3\alpha \sin \beta \\ &+ \sqrt{3}(\mu_{22} - \mu_{11}) \sin 2\alpha \sin 2\beta, \end{aligned} \quad (\text{A8})$$

$$\begin{aligned} \text{Im}[V_{12}] &= 4t_{12} \sin \alpha (\cos \alpha - \cos \beta) \\ &+ 4\mu_{12} \sin 2\alpha (\cos 2\alpha - \cos 2\beta), \end{aligned} \quad (\text{A9})$$

and

$$\begin{aligned} V_{22} &= \varepsilon_2 + (3t_{11} + t_{22}) \cos \alpha \cos \beta + 2t_{22} \cos 2\alpha \\ &+ 2r_{11}(2 \cos 3\alpha \cos \beta + \cos 2\beta) \\ &+ \frac{2}{\sqrt{3}}r_{12}(4 \cos 3\alpha \cos \beta - \cos 2\beta) \\ &+ (3\mu_{11} + \mu_{22}) \cos 2\alpha \cos 2\beta + 2\mu_{22} \cos 4\alpha. \end{aligned} \quad (\text{A10})$$

Here,  $(\alpha, \beta) = (\frac{1}{2}k_x a, \frac{\sqrt{3}}{2}k_y a)$  with a lattice constant  $a$ . By fitting the first-principle band structure in the local-density approximation, these TB parameters (in units of eV) for monolayer MoS<sub>2</sub> are chosen as  $\varepsilon_1 = 0.820$ ,  $\varepsilon_2 = 1.931$ ,  $t_0 = -0.176$ ,  $t_1 = -0.101$ ,  $t_2 = 0.531$ ,  $t_{11} = 0.084$ ,  $t_{12} = 0.169$ ,  $t_{22} = 0.070$ ,  $r_0 = 0.070$ ,  $r_1 = -0.252$ ,  $r_2 = 0.084$ ,  $r_{11} = 0.019$ ,  $r_{12} = 0.093$ ,  $u_0 = -0.043$ ,  $u_1 = 0.047$ ,  $u_2 = 0.005$ ,  $u_{11} = 0.304$ ,  $u_{12} = -0.192$ ,  $u_{22} = -0.162$ , and  $a = 3.129$  Å.

The second term in Eq. (1) refers to the SOC Hamiltonian with splitting strength set as  $\lambda = 0.073$  eV. The matrix form of  $L_z$ , which is  $z$  component of orbital angular momentum in bases of  $\{d_{z^2}, d_{xy}, d_{x^2-y^2}\}$ , is given by

$$L_z = \begin{pmatrix} 0 & 0 & 0 \\ 0 & 0 & 2i \\ 0 & -2i & 0 \end{pmatrix}. \quad (\text{A11})$$

The third term in Eq. (1) refers to the Ising SOC in the CBs and is expressed as [30]

$$H_c(\mathbf{k}) = \begin{pmatrix} \gamma(\mathbf{k}) & 0 & 0 \\ 0 & 0 & 0 \\ 0 & 0 & 0 \end{pmatrix}, \quad (\text{A12})$$

where

$$\gamma(\mathbf{k}) = -\frac{2\beta_c}{3\sqrt{3}}[\sin 2\alpha - 2 \sin \alpha \cos \beta] \quad (\text{A13})$$

with the energy splitting  $2\beta_c = -3$  meV for MoS<sub>2</sub>.

In the Rashba SOC Hamiltonian, the functions  $f_x(\mathbf{k})$  and  $f_y(\mathbf{k})$  are given by

$$f_x(\mathbf{k}) = \sin 2\alpha + \sin \alpha \cos \beta \quad (\text{A14})$$

and

$$f_y(\mathbf{k}) = \sqrt{3} \sin \beta \cos \alpha. \quad (\text{A15})$$

## APPENDIX B: DENSITY-MATRIX EQUATION IN ATOMIC ORBITAL BASIS

In this appendix we provide more details about the derivation of density-matrix equations in the representation of linear combination of atomic orbitals. The correct choice of a crystal basis function needs to take the Bloch sum form of atomic orbitals  $\phi_{\alpha n}$ , given by

$$|B_{\alpha,n,\mathbf{k}}\rangle = \frac{1}{\sqrt{N}} \sum_{\mathbf{R}} e^{i\mathbf{k}\cdot(\mathbf{R}+\boldsymbol{\tau}_n)} |\phi_{\alpha n}(\mathbf{r} - \mathbf{R} - \boldsymbol{\tau}_n)\rangle, \quad (\text{B1})$$

where  $n$  represents one atom with a location  $\boldsymbol{\tau}_n$  relative to the primitive unit cell, and  $\alpha$  specifies the orbital shape ( $s$ ,  $p$ , etc.) on this atom  $n$ . Here, there are  $N$  unit cells in the crystal and the sum runs over all lattice vectors  $\mathbf{R}$ . Note that Eq. (B1) can be applied to a general lattice structure for which the home unit cell may include several atoms and each atom may have several orbitals.

Considering the length-gauge Hamiltonian in the density-matrix equation, we should adopt the basis function Eq. (B1) under the acceleration theorem where the lattice momentum is shifted by the vector potential of laser pulse. In this case, the reduced density operator for an initial crystal momentum  $\mathbf{k}_0$  is written as

$$\rho^{\mathbf{k}_0}(t) = \sum_{\beta m, \alpha n} \rho_{\beta m, \alpha n}^{\mathbf{k}_0}(t) |B_{\beta m, \mathbf{k}(t)}\rangle \langle B_{\alpha n, \mathbf{k}(t)}|, \quad (\text{B2})$$

with the time-dependent momentum  $\mathbf{k}(t) = \mathbf{k}_0 + \mathbf{A}(t)$ .

It is helpful to firstly calculate

$$\begin{aligned} i \frac{d}{dt} |B_{\alpha,n,\mathbf{k}(t)}\rangle &= i \frac{1}{\sqrt{N}} \frac{d}{dt} \sum_{\mathbf{R}} e^{i\mathbf{k}(t)\cdot(\mathbf{R}+\boldsymbol{\tau}_n)} |\phi_{\alpha n}(\mathbf{r} - \mathbf{R} - \boldsymbol{\tau}_n)\rangle \\ &= -\mathbf{E}(t) \cdot |\mathbf{A}_{\alpha,n,\mathbf{k}(t)}\rangle + \mathbf{E}(t) \cdot \mathbf{r} |B_{\alpha,n,\mathbf{k}(t)}\rangle, \end{aligned} \quad (\text{B3})$$

where we have defined

$$\begin{aligned} |\mathbf{A}_{\alpha,n,\mathbf{k}(t)}\rangle &= \frac{1}{\sqrt{N}} \sum_{\mathbf{R}} (\mathbf{r} - \mathbf{R} - \boldsymbol{\tau}_n) e^{i\mathbf{k}(t)\cdot(\mathbf{R}+\boldsymbol{\tau}_n)} |\phi_{\alpha n}(\mathbf{r} - \mathbf{R} - \boldsymbol{\tau}_n)\rangle. \end{aligned} \quad (\text{B4})$$

Their conjugate expressions have the form

$$i \frac{d}{dt} \langle B_{\alpha,n,\mathbf{k}(t)}| = \mathbf{E}(t) \cdot \langle \mathbf{A}_{\alpha,n,\mathbf{k}(t)}| - \mathbf{E}(t) \cdot \langle B_{\alpha,n,\mathbf{k}(t)}| \mathbf{r}, \quad (\text{B5})$$

and

$$\begin{aligned} \langle \mathbf{A}_{\alpha,n,\mathbf{k}(t)}| &= \frac{1}{\sqrt{N}} \sum_{\mathbf{R}} \langle \phi_{\alpha n}(\mathbf{r} - \mathbf{R} - \boldsymbol{\tau}_n) | (\mathbf{r} - \mathbf{R} - \boldsymbol{\tau}_n) e^{-i\mathbf{k}(t)\cdot(\mathbf{R}+\boldsymbol{\tau}_n)}. \end{aligned} \quad (\text{B6})$$

Differentiating both sides of Eq. (B2) with respect to  $t$  and making use of Eqs. (B3)–(B6), we can get

$$\begin{aligned} i \frac{d}{dt} \rho^{\mathbf{k}_0}(t) &= \sum_{\beta m, \alpha n} i \frac{d \rho_{\beta m, \alpha n}^{\mathbf{k}_0}(t)}{dt} |B_{\beta m, \mathbf{k}(t)}\rangle \langle B_{\alpha n, \mathbf{k}(t)}| \\ &\quad - \mathbf{E}(t) \cdot \left[ \sum_{\beta m, \alpha n} \rho_{\beta m, \alpha n}^{\mathbf{k}_0}(t) |\mathbf{A}_{\beta m, \mathbf{k}(t)}\rangle \langle B_{\alpha n, \mathbf{k}(t)}| \right. \\ &\quad \left. - |B_{\beta m, \mathbf{k}(t)}\rangle \langle \mathbf{A}_{\alpha n, \mathbf{k}(t)}| \right] + \mathbf{E}(t) \cdot [\mathbf{r}, \rho^{\mathbf{k}_0}(t)]. \end{aligned} \quad (\text{B7})$$

By comparing Eq. (3) and Eq. (B7), we arrive at

$$\begin{aligned} \sum_{\beta m, \alpha n} i \frac{d \rho_{\beta m, \alpha n}^{\mathbf{k}_0}(t)}{dt} |B_{\beta m, \mathbf{k}(t)}\rangle \langle B_{\alpha n, \mathbf{k}(t)}| &= [H_0, \rho^{\mathbf{k}_0}(t)] + \mathbf{E}(t) \cdot \left[ \sum_{\beta m, \alpha n} \rho_{\beta m, \alpha n}^{\mathbf{k}_0}(t) \right. \\ &\quad \left. \times |\mathbf{A}_{\beta m, \mathbf{k}(t)}\rangle \langle B_{\alpha n, \mathbf{k}(t)}| - |B_{\beta m, \mathbf{k}(t)}\rangle \langle \mathbf{A}_{\alpha n, \mathbf{k}(t)}| \right]. \end{aligned} \quad (\text{B8})$$

After performing the inner product  $\langle B_{\beta' m', \mathbf{k}(t)}| \cdot |B_{\alpha' n', \mathbf{k}(t)}\rangle$  at both sides of Eq. (B8), we can obtain the equation of motion for density matrix  $\rho_{\beta m, \alpha n}^{\mathbf{k}_0}(t)$  as

$$\begin{aligned} i \sum_{\beta m, \alpha n} S_{\beta' m', \beta m} \frac{d \rho_{\beta m, \alpha n}^{\mathbf{k}_0}(t)}{dt} S_{\alpha n, \alpha' n'} &= \sum_{\beta m, \alpha n} [H_{\beta' m', \beta m} \rho_{\beta m, \alpha n}^{\mathbf{k}_0}(t) S_{\alpha n, \alpha' n'} \\ &\quad - S_{\beta' m', \beta m} \rho_{\beta m, \alpha n}^{\mathbf{k}_0}(t) H_{\alpha n, \alpha' n'}] + \mathbf{E}(t) \\ &\quad \cdot \left[ \sum_{\beta m, \alpha n} \mathbf{d}_{\beta' m', \beta m}(\mathbf{k}) \rho_{\beta m, \alpha n}^{\mathbf{k}_0}(t) S_{\alpha n, \alpha' n'} \right. \\ &\quad \left. - S_{\beta' m', \beta m} \rho_{\beta m, \alpha n}^{\mathbf{k}_0}(t) \mathbf{d}_{\alpha n, \alpha' n'}(\mathbf{k}) \right], \end{aligned} \quad (\text{B9})$$

where the relevant matrix elements are explicitly given by

$$\begin{aligned} S_{\beta' m', \beta m}(\mathbf{k}) &= \langle B_{\beta' m', \mathbf{k}} | B_{\beta m, \mathbf{k}} \rangle \\ &= \sum_{\mathbf{R}} e^{i\mathbf{k}\cdot\mathbf{R} m'} \langle \phi_{\beta' m'}(\mathbf{r}) | \phi_{\beta m}(\mathbf{r} - \mathbf{R}_{m' m}) \rangle, \end{aligned} \quad (\text{B10})$$

$$\begin{aligned} H_{\beta' m', \beta m}(\mathbf{k}) &= \langle B_{\beta' m', \mathbf{k}} | H_0 | B_{\beta m, \mathbf{k}} \rangle \\ &= \sum_{\mathbf{R}} e^{i\mathbf{k}\cdot\mathbf{R} m'} \langle \phi_{\beta' m'}(\mathbf{r}) | H_0 | \phi_{\beta m}(\mathbf{r} - \mathbf{R}_{m' m}) \rangle, \end{aligned} \quad (\text{B11})$$

$$\begin{aligned} \mathbf{d}_{\beta'm',\beta m}(\mathbf{k}) &= \langle B_{\beta'm',\mathbf{k}} | \mathbf{A}_{\beta m,\mathbf{k}} \rangle \\ &= \sum_{\mathbf{R}} e^{i\mathbf{k}\cdot\mathbf{R}_{m'm}} \langle \phi_{\beta'm'}(\mathbf{r} + \mathbf{R}_{m'm}) | \mathbf{r} | \phi_{\beta m}(\mathbf{r}) \rangle, \end{aligned} \quad (\text{B12})$$

with the definition  $\mathbf{R}_{m'm} = \mathbf{R} + \boldsymbol{\tau}_m - \boldsymbol{\tau}_{m'}$ .

We can rewrite Eq. (B9) in a compact matrix form without displaying the indices,

$$i \frac{d\boldsymbol{\rho}^{\mathbf{k}_0}(t)}{dt} = \mathbf{S}^{-1}(\mathbf{k}) \bar{\mathbf{H}}(\mathbf{k}) \boldsymbol{\rho}^{\mathbf{k}_0}(t) - \boldsymbol{\rho}^{\mathbf{k}_0}(t) \bar{\mathbf{H}}(\mathbf{k}) \mathbf{S}^{-1}(\mathbf{k}), \quad (\text{B13})$$

where the interaction Hamiltonian matrix reads

$$\bar{\mathbf{H}}(\mathbf{k}) = \mathbf{H}(\mathbf{k}) + \mathbf{E}(t) \cdot \mathbf{d}(\mathbf{k}). \quad (\text{B14})$$

In the above two equations,  $\mathbf{S}(\mathbf{k})$  is called the overlap matrix,  $\mathbf{H}(\mathbf{k})$  is the tight-binding Hamiltonian matrix, and  $\mathbf{d}(\mathbf{k})$  is the dipole transition matrix. These matrix elements, given by Eqs. (B10)–(B12), automatically have continuous phase when electrons move along a certain path in  $\mathbf{k}$  space. Thus, Eq. (B13) provides the advantage of avoiding the random phase problem which usually arises from the LG density-matrix equation formulated in the Bloch eigenstate basis [51–54]. In addition, it has also good numerical stability even if in the presence of degenerate bands and band crossings. It should be noted that our approach is consistent with the one implemented in the basis of maximally localized Wannier functions [55].

In order to further simplify Eq. (B13), we can make some assumptions based on tight-binding approximation that atomic orbitals are normalized and their overlapping between different atomic sites is ignored. Under this condition,  $\mathbf{S}(\mathbf{k})$  becomes identity matrix and we have [56]

$$\begin{aligned} \langle \phi_{\beta'm'}(\mathbf{r} + \mathbf{R}_{m'm}) | \mathbf{r} | \phi_{\beta m}(\mathbf{r}) \rangle \\ = \delta_{\mathbf{R},0} \delta_{m'm} (-\mathbf{R}_{m'm} \delta_{\beta'\beta} + \tilde{\mathbf{d}}_{\beta'\beta}^m), \end{aligned} \quad (\text{B15})$$

where  $\tilde{\mathbf{d}}_{\beta'\beta}^m = \langle \phi_{\beta'm'} | \mathbf{r} | \phi_{\beta m}(\mathbf{r}) \rangle$  represents the intra-atomic dipole matrix element at atom  $m$ . It follows that  $\mathbf{d}(\mathbf{k})$  becomes zero if substituting Eq. (B15) into Eq. (B12) and when selection rule forbids the intra-atomic dipole transition. As a result, Eq. (B13) finally reduces to Eq. (5), as given in the main text.

### APPENDIX C: 22-BAND TIGHT-BINDING MODEL FOR CALCULATING RASHBA EFFECT

In this appendix we employ a relatively complicated tight-binding model for calculating the Rashba effect in monolayer MoS<sub>2</sub>. The purpose is to obtain an explicit dependence of Rashba SOC on the perpendicular control electric field, and simultaneously the results provided by the two different tight-binding models can be cross-checked to make our conclusion more convincing.

We start from a spinless case in which all five  $d$  orbitals of Mo atom, and three  $p$  orbitals for each of two S atoms in the top (t) and bottom (b) sublayer are taken into account to construct the 11-band tight-binding Hamiltonian [57]. Here, the interaction term contains six Mo-S and one S (top)-S (bottom) nearest-neighbor hopping in the same unit cell, and six Mo-Mo and six S-S next-to-nearest-neighbor hopping between the unit cell and the adjacent cells. All hopping amplitudes are expressed in terms of Slater-Koster (SK) mechanism, which

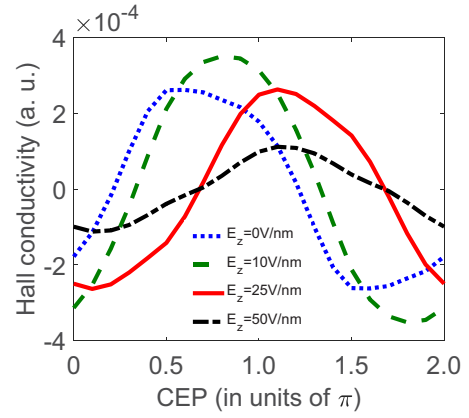


FIG. 9. Comparison of CEP-dependent Hall conductivity, calculated for four different external electric fields perpendicular to monolayer surface:  $E_z = 0$  V/nm (blue dot),  $E_z = 10$  V/nm (green dashed),  $E_z = 25$  V/nm (red solid) and  $E_z = 50$  V/nm (black-dashed-dotted). The driving light has the central wavelength  $\lambda = 8 \mu\text{m}$ , pulse duration 27 fs, and the peak intensity  $I_0 = 0.1 \text{ TW/cm}^2$ .

are finally attributed to some bond parameters. In our calculation, all SK parameters are taken from the second column of Table 6 in Ref. [57].

The Rashba-type SOC can naturally occur when applying an electric field perpendicular to the monolayer surface, which induces the asymmetry of the side potentials. The basic idea for incorporating the effect of external electric field in the tight-binding model relies on modification of the on-site energies of atoms in three MoS<sub>2</sub> sublayers [58]. We introduce an additional on-site potential for the top (bottom) S-atom layers as  $V_{t,b} = \pm E_z d/2$ , where  $d = 0.32 \text{ nm}$  is the monolayer thickness and  $E_z$  is the perpendicular electric field. It is then straightforward to insert the SOC term by adding intra-atomic LS coupling contribution as  $H_{SO} = \sum_a \lambda_a \mathbf{L}_a \cdot \mathbf{S}_a$ , where  $\lambda_a$  represents the intrinsic SOC strength for Mo atom  $\lambda_{Mo} = 0.086 \text{ eV}$  and for S atom  $\lambda_S = 0.052 \text{ eV}$ . Thus, this kind of treatment can double orbital numbers by assigning each orbital a spin component, and extend the spinless system to full  $22 \times 22$  tight-binding Hamiltonian with  $E_z$  serving as a controllable parameter that describes the Rashba coupling strength. Finally, we incorporate the full  $22 \times 22$  Hamiltonian into the Liouville–von Neumann Eq. (5) for simulating subcycle valley polarization dynamics and calculating the CEP-dependent valley Hall conductivity, as the same procedure implemented for six-band model discussed in the main text.

Figure 9 shows calculated Hall conductivity  $\sigma_{xy}$  as a function of CEP, under four different perpendicular electric fields:  $E_z = 0$  V/nm (blue dot),  $E_z = 10$  V/nm (green dashed),  $E_z = 25$  V/nm (red solid) and  $E_z = 50$  V/nm (black-dashed-dotted). One can see that the CEP-dependent  $\sigma_{xy}$  for the four cases all exhibit near-sine oscillations, with the phase determined by the amplitude of perpendicular electric field. The simulation result is similar to the one reported in Fig. 3. In other words, different Rashba coupling strengths due to applying different perpendicular electric fields can indeed result in an important phase shift, which yields the consistent conclusion with those results obtained from the six-band Hamiltonian Eq. (1).

- [1] J. Lloyd-Hughes, P. M. Oppeneer, T. Pereira Dos Santos, A. Schleife, S. Meng, M. A. Sentef, M. Ruggenthaler, A. Rubio, I. Radu, M. Murnane, X. Shi, H. Kapteyn, B. Stadtmuller, K. M. Dani, F. H. da Jornada, E. Prinz, M. Aeschlimann, R. L. Milot, M. Burdanova, J. Boland, T. Cocker, and F. Hegmann, The 2021 ultrafast spectroscopic probes of condensed matter roadmap, *J. Phys.: Condens. Matter* **33**, 353001 (2021).
- [2] R. Borrego-Varillas, M. Lucchini, and M. Nisoli, Attosecond spectroscopy for the investigation of ultrafast dynamics in atomic, molecular and solid-state physics, *Rep. Prog. Phys.* **85**, 066401 (2022).
- [3] A. de la Torre, D. M. Kennes, M. Claassen, S. Gerber, J. W. McIver, and M. A. Sentef, Colloquium: Nonthermal pathways to ultrafast control in quantum materials, *Rev. Mod. Phys.* **93**, 041002 (2021).
- [4] E. Goulielmakis, V. S. Yakovlev, A. L. Cavalieri, M. Uiberacker, V. Pervak, A. Apolonski, R. Kienberger, U. Kleineberg, and F. Krausz, Attosecond control and measurement: Lightwave electronics, *Science* **317**, 769 (2007).
- [5] T. Higuchi, C. Heide, K. Ullmann, H. B. Weber, and P. Hommelhoff, Light-field-driven currents in graphene, *Nature (London)* **550**, 224 (2017).
- [6] T. Boolakee, C. Heide, A. Garzon-Ramirez, H. B. Weber, I. Franco, and P. Hommelhoff, Light-field control of real and virtual charge carriers, *Nature (London)* **605**, 251 (2022).
- [7] M. Ossianer, K. Golyari, K. Scharl, L. Lehnert, F. Siegrist, J. P. Burger, D. Zimin, J. A. Gessner, M. Weidman, I. Floss, V. Smejkal, S. Donsa, C. Lemell, F. Libisch, N. Karpowicz, J. Burgdorfer, F. Krausz, and M. Schultze, The speed limit of optoelectronics, *Nat. Commun.* **13**, 1620 (2022).
- [8] F. Krausz and M. I. Stockman, Attosecond metrology: From electron capture to future signal processing, *Nat. Photonics* **8**, 205 (2014).
- [9] J. R. Schaibley, H. Y. Yu, G. Clark, P. Rivera, J. S. Ross, K. L. Seyler, W. Yao, and X. D. Xu, Valleytronics in 2D materials, *Nat. Rev. Mater* **1**, 16055 (2016).
- [10] L. Yue, R. Hollinger, C. B. Uzundal, B. Nebgen, Z. Gan, E. Najafidehaghani, A. George, C. Spielmann, D. Kartashov, A. Turchanin, D. Y. Qiu, M. B. Gaarde, and M. Zuerch, Signatures of Multiband Effects in High-Harmonic Generation in Monolayer MoS<sub>2</sub>, *Phys. Rev. Lett.* **129**, 147401 (2022).
- [11] N. Yoshikawa, K. Nagai, K. Uchida, Y. Takaguchi, S. Sasaki, Y. Miyata, and K. Tanaka, Interband resonant high-harmonic generation by valley polarized electron-hole pairs, *Nat. Commun.* **10**, 3709 (2019).
- [12] C. Liu, Y. Zheng, Z. Zeng, and R. Li, Polarization-resolved analysis of high-order harmonic generation in monolayer MoS<sub>2</sub>, *New J. Phys.* **22**, 073046 (2020).
- [13] Y.-L. He, J. Guo, F.-Y. Gao, and X.-S. Liu, Dynamical symmetry and valley-selective circularly polarized high-harmonic generation in monolayer molybdenum disulfide, *Phys. Rev. B* **105**, 024305 (2022).
- [14] H. Liu, Y. Li, Y. S. You, S. Ghimire, T. F. Heinz, and D. A. Reis, High-harmonic generation from an atomically thin semiconductor, *Nat. Phys.* **13**, 262 (2017).
- [15] X. Xu, W. Yao, D. Xiao, and T. F. Heinz, Spin and pseudospins in layered transition metal dichalcogenides, *Nat. Phys.* **10**, 343 (2014).
- [16] S. A. Vitale, D. Nezhich, J. O. Varghese, P. Kim, N. Gedik, P. Jarillo-Herrero, D. Xiao, and M. Rothschild, Valleytronics: Opportunities, challenges, and paths forward, *Small* **14**, e1801483 (2018).
- [17] Á. Jiménez-Galán, R. E. F. Silva, O. Smirnova, and M. Ivanov, Lightwave control of topological properties in 2D materials for sub-cycle and non-resonant valley manipulation, *Nat. Photonics* **14**, 728 (2020).
- [18] M. S. Mrudul, Á. Jiménez-Galán, M. Ivanov, and G. Dixit, Light-induced valleytronics in pristine graphene, *Optica* **8**, 422 (2021).
- [19] Á. Jiménez-Galán, R. E. F. Silva, O. Smirnova, and M. Ivanov, Sub-cycle valleytronics: Control of valley polarization using few-cycle linearly polarized pulses, *Optica* **8**, 277 (2021).
- [20] S. A. Oliaei Motlagh, F. Nematollahi, A. Mitra, A. J. Zafar, V. Apalkov, and M. I. Stockman, Ultrafast optical currents in gapped graphene, *J. Phys.: Condens. Matter* **32**, 065305 (2020).
- [21] C. Lefebvre, D. Gagnon, F. Fillion-Gourdeau, and S. MacLean, Carrier-envelope phase effects in graphene, *J. Opt. Soc. Am. B* **35**, 958 (2018).
- [22] G. Bergmann, The anomalous Hall effect, *Phys. Today* **32**(8), 25 (1979).
- [23] A. Kormányos, V. Zólyomi, N. D. Drummond, and G. Burkard, Erratum: Spin-Orbit Coupling, Quantum Dots, and Qubits in Monolayer Transition Metal Dichalcogenides [Phys. Rev. X **4**, 011034 (2014)], *Phys. Rev. X* **4**, 039901(E) (2014).
- [24] Q.-F. Yao, J. Cai, W.-Y. Tong, S.-J. Gong, J.-Q. Wang, X. Wan, C.-G. Duan, and J. H. Chu, Manipulation of the large Rashba spin splitting in polar two-dimensional transition-metal dichalcogenides, *Phys. Rev. B* **95**, 165401 (2017).
- [25] Y. C. Cheng, Z. Y. Zhu, M. Tahir, and U. Schwingenschlögl, Spin-orbit-induced spin splittings in polar transition metal dichalcogenide monolayers, *Europhys. Lett.* **102**, 57001 (2013).
- [26] C. L. Yang, H. T. He, L. Ding, L. J. Cui, Y. P. Zeng, J. N. Wang, and W. K. Ge, Spectral Dependence of Spin Photocurrent and Current-Induced Spin Polarization in an InGaAs/InAlAs Two-Dimensional Electron Gas, *Phys. Rev. Lett.* **96**, 186605 (2006).
- [27] I. Markovic, C. A. Hooley, O. J. Clark, F. Mazzola, M. D. Watson, J. M. Riley, K. Volckaert, K. Underwood, M. S. Dyer, P. A. E. Murgatroyd, K. J. Murphy, P. L. Fevre, F. Bertran, J. Fujii, I. Vobornik, S. Wu, T. Okuda, J. Alaria, and P. D. C. King, Weyl-like points from band inversions of spin-polarised surface states in NbGeSb, *Nat. Commun.* **10**, 5485 (2019).
- [28] S. LaShell, B. A. McDougall, and E. Jensen, Spin Splitting of an Au(111) Surface State Band Observed with Angle Resolved Photoelectron Spectroscopy, *Phys. Rev. Lett.* **77**, 3419 (1996).
- [29] C. R. Ast, J. Henk, A. Ernst, L. Moreschini, M. C. Falub, D. Pacile, P. Bruno, K. Kern, and M. Grioni, Giant Spin Splitting through Surface Alloying, *Phys. Rev. Lett.* **98**, 186807 (2007).
- [30] B. T. Zhou, K. Taguchi, Y. Kawaguchi, Y. Tanaka, and K. T. Law, Spin-orbit coupling induced valley Hall effects in transition-metal dichalcogenides, *Commun. Phys.* **2**, 26 (2019).
- [31] M. Lysne, Y. Murakami, M. Schüler, and P. Werner, High-harmonic generation in spin-orbit coupled systems, *Phys. Rev. B* **102**, 081121(R) (2020).
- [32] E. Cappelluti, R. Roldán, J. A. Silva-Guillén, P. Ordejón, and F. Guinea, Tight-binding model and direct-gap/indirect-gap transition in single-layer and multilayer MoS<sub>2</sub>, *Phys. Rev. B* **88**, 075409 (2013).

- [33] G.-B. Liu, W.-Y. Shan, Y. Yao, W. Yao, and D. Xiao, Three-band tight-binding model for monolayers of group-VIB transition metal dichalcogenides, *Phys. Rev. B* **88**, 085433 (2013).
- [34] G. A. H. Schober, K. U. Giering, M. M. Scherer, C. Honerkamp, and M. Salmhofer, Functional renormalization and mean-field approach to multiband systems with spin-orbit coupling: Application to the Rashba model with attractive interaction, *Phys. Rev. B* **93**, 115111 (2016).
- [35] B. T. Zhou, C.-P. Zhang, and K. T. Law, Highly Tunable Non-linear Hall Effects Induced by Spin-Orbit Couplings in Strained Polar Transition-Metal Dichalcogenides, *Phys. Rev. Appl.* **13**, 024053 (2020).
- [36] K. Kośmider, J. W. González, and J. Fernández-Rossier, Large spin splitting in the conduction band of transition metal dichalcogenide monolayers, *Phys. Rev. B* **88**, 245436 (2013).
- [37] J. M. Lu, O. Zheliuk, I. Leermakers, N. F. Yuan, U. Zeitler, K. T. Law, and J. T. Ye, Evidence for two-dimensional Ising superconductivity in gated MoS<sub>2</sub>, *Science* **350**, 1353 (2015).
- [38] K. V. Shanavas, Z. S. Popović, and S. Satpathy, Theoretical model for Rashba spin-orbit interaction in electrons, *Phys. Rev. B* **90**, 165108 (2014).
- [39] L. Yue and M. B. Gaarde, Introduction to theory of high-harmonic generation in solids: Tutorial, *J. Opt. Soc. Am. B* **39**, 535 (2022).
- [40] J. Wilhelm, P. Grössing, A. Seith, J. Crewse, M. Nitsch, L. Weigl, C. Schmid, and F. Evers, Semiconductor Bloch-equations formalism: Derivation and application to high-harmonic generation from Dirac fermions, *Phys. Rev. B* **103**, 125419 (2021).
- [41] G. Vampa, C. R. McDonald, G. Orlando, D. D. Klug, P. B. Corkum, and T. Brabec, Theoretical Analysis of High-Harmonic Generation in Solids, *Phys. Rev. Lett.* **113**, 073901 (2014).
- [42] J. Chen, C. Liu, Z. Zeng, and R. Li, Control of ultrafast photocurrent in twisted bilayer graphene by circularly polarized few-cycle lasers, *Phys. Rev. B* **105**, 014309 (2022).
- [43] A. Schiffrin, T. Paasch-Colberg, N. Karpowicz, V. Apalkov, D. Gerster, S. Muhlbrandt, M. Korbman, J. Reichert, M. Schultze, S. Holzner, J. V. Barth, R. Kienberger, R. Ernstorfer, V. S. Yakovlev, M. I. Stockman, and F. Krausz, Addendum: Optical-field-induced current in dielectrics, *Nature (London)* **493**, 70 (2013).
- [44] C. Heide, T. Boolakee, T. Higuchi, H. B. Weber, and P. Hommelhoff, Interaction of carrier envelope phase-stable laser pulses with graphene: The transition from the weak-field to the strong-field regime, *New J. Phys.* **21**, 045003 (2019).
- [45] D. Xiao, G. B. Liu, W. Feng, X. Xu, and W. Yao, Coupled Spin and Valley Physics in Monolayers of MoS<sub>2</sub> and Other Group-VI Dichalcogenides, *Phys. Rev. Lett.* **108**, 196802 (2012).
- [46] K. F. Mak, K. L. McGill, J. Park, and P. L. McEuen, The valley Hall effect in MoS<sub>2</sub> transistors, *Science* **344**, 1489 (2014).
- [47] D. Xiao, M.-C. Chang, and Q. Niu, Berry phase effects on electronic properties, *Rev. Mod. Phys.* **82**, 1959 (2010).
- [48] S. N. Shevchenko, S. Ashhab, and F. Nori, Landau-Zener-Stückelberg interferometry, *Phys. Rep.* **492**, 1 (2010).
- [49] E. Wu, C. Zhang, Z. Wang, and C. Liu, Waveform control of currents in graphene by chirped few-cycle lasers, *New J. Phys.* **22**, 033016 (2020).
- [50] M. S. Wismer, S. Y. Kruchinin, M. Ciappina, M. I. Stockman, and V. S. Yakovlev, Strong-Field Resonant Dynamics in Semiconductors, *Phys. Rev. Lett.* **116**, 197401 (2016).
- [51] J. Li, X. Zhang, S. Fu, Y. Feng, B. Hu, and H. Du, Phase invariance of the semiconductor Bloch equations, *Phys. Rev. A* **100**, 043404 (2019).
- [52] L. Yue and M. B. Gaarde, Structure gauges and laser gauges for the semiconductor Bloch equations in high-order harmonic generation in solids, *Phys. Rev. A* **101**, 053411 (2020).
- [53] S. Jiang, C. Yu, J. Chen, Y. Huang, R. Lu, and C. D. Lin, Smooth periodic gauge satisfying crystal symmetry and periodicity to study high-harmonic generation in solids, *Phys. Rev. B* **102**, 155201 (2020).
- [54] L. H. Thong, C. Ngo, H. T. Duc, X. Song, and T. Meier, Microscopic analysis of high harmonic generation in semiconductors with degenerate bands, *Phys. Rev. B* **103**, 085201 (2021).
- [55] R. E. F. Silva, F. Martín, and M. Ivanov, High harmonic generation in crystals using maximally localized Wannier functions, *Phys. Rev. B* **100**, 195201 (2019).
- [56] M. Cruz, M. R. Beltrán, C. Wang, J. Tagüeña-Martínez, and Y. G. Rubo, Supercell approach to the optical properties of porous silicon, *Phys. Rev. B* **59**, 15381 (1999).
- [57] E. Ridolfi, D. Le, T. S. Rahman, E. R. Mucciolo, and C. H. Lewenkopf, A tight-binding model for MoS<sub>2</sub> monolayers, *J. Phys.: Condens. Matter* **27**, 365501 (2015).
- [58] J. Pawłowski, Spin-valley system in a gated MoS<sub>2</sub>-monolayer quantum dot, *New J. Phys.* **21**, 123029 (2019).